



## ISTITUTO NAZIONALE DI RICERCA METROLOGICA Repository Istituzionale

Machine-Learning-Assisted Design of a Robust Biomimetic Radiative Cooling Metamaterial

This is the author's submitted version of the contribution published as:

*Original*

Machine-Learning-Assisted Design of a Robust Biomimetic Radiative Cooling Metamaterial / Ding, Zm; Li, X; Ji, Qx; Zhang, Yc; Li, Hl; Zhang, Hl; Pattelli, L; Li, Y; Xu, Hb; Zhao, Jp. - In: ACS MATERIALS LETTERS. - ISSN 2639-4979. - (2024). [10.1021/acsmaterialslett.4c00337]

*Availability:*

This version is available at: 11696/81019 since: 2025-03-02T14:07:47Z

*Publisher:*

AMER CHEMICAL SOC

*Published*

DOI:10.1021/acsmaterialslett.4c00337

*Terms of use:*

This article is made available under terms and conditions as specified in the corresponding bibliographic description in the repository

*Publisher copyright*

(Article begins on next page)

# Machine-Learning-Assisted Design of a Robust Biomimetic Radiative Cooling Metamaterial

Zhenmin Ding, Xin Li, Qingxiang Ji \*, Yunce Zhang, Honglin Li, Hulin Zhang,

Lorenzo Pattelli, Yao Li, Hongbo Xu \*, Jiupeng Zhao \*

**Abstract:** Recently, biomimetic photonic structural materials have significantly advanced the radiative cooling performance of designed materials. However, the biomimetic metamaterials have largely concentrated on the biological radiative cooling mechanism, with little effort to investigate sensitive parameter variations. Additionally, traditional numerical methods are not only costly and laborious, but also challenging to uncover optimal solutions, often yielding high-performance microstructures with a narrow range of preparation intervals. To address this, machine learning (ML) was introduced into the design of a biomimetic photonic structure based on the *Batocera Lineolata* Hope, and silicon dioxide (SiO<sub>2</sub>) was chosen as the substrate material. By employing a deep learning model, we can understand the correlation between biomimetic metamaterial and their corresponding spectral responses. We managed to attain a large range ( $H/D_{\text{bottom}}$  between 0.8 and 2.4) of optimal performance parameters for a truncated cone array, which resulted in an average emissivity of 0.985. Subsequently, the fabricated truncated cone array samples showed a temperature drop of about 8.3 °C at midday in experiments. By taking the above data-driven approach, the process of designing and optimizing robust biomimetic radiative cooling metamaterials can be expedited, making it an ideal

option for standardized passive radiative cooling applications.

**Keywords:** *Biomimetic photonic materials, Machine learning, Photonic design, Infrared emissivity, Radiative cooler*

## **1. Introduction**

Metamaterials created through photonic micro/nanostructures have been extensively studied in the fields of thermal manipulation, i.e., thermal camouflage, radiative cooling, signaling, and so forth.<sup>1-3</sup> Of particular interest is the imitation of microstructures based on natural creatures, as this allows for the direct analysis of the microstructure's functionality through the external behavior of plants and animals.<sup>4-9</sup> The application of biomimetic photonic structures in the realm of infrared radiation is a promising trend, which can greatly enhance the radiative cooling performance of designed materials.<sup>10-11</sup> This form of passive cooling, different from active cooling systems such as air conditioning, requires no extra energy input and produces no pollution, showing a significant contribution to energy conservation and environmental protection.<sup>12-13</sup>

Researchers have developed materials and systems that are proficient in radiative cooling by examining the heat radiation characteristics of living organisms. Shi et al.<sup>14</sup> first discovered that the Sahara silver ants have a remarkable radiative cooling feature because of the densely packed triangular hairs on their heads. Xie et al.<sup>15</sup> demonstrated that the scales section of the white beetle (*Goliathus goliatus*) in tropical rainforests has shell/hollow cylinder structures that can suppress reflection in the mid-infrared band, thereby augmenting the emissivity. Some other organisms, like various types of butterflies,<sup>16-17</sup> golden cicadas,<sup>18</sup> and long-horned beetles,<sup>19</sup> also

exhibit enlarged emissivity in the mid-infrared band by reducing the reflection. Current metamaterial design primarily draws on the biological radiative cooling mechanism, neglecting the exploration of the primary structural parameters in practical preparation. This method, however, does not establish a connection between the sample spectra and the sensitive parameters, and thus cannot be used to provide a useful guide for practical preparations.

The preparation of biomimetic photonic materials typically involves complex processing, for which numerical methods provide an effective way to predict the optical response of intricate artificial structures.<sup>20-22</sup> For example, our previous work has demonstrated that the emissivity of microstructured samples is optimized when the period of the microcone arrays is 1-2  $\mu\text{m}$  and the aspect ratio is greater than 1.5.<sup>23</sup> Numerical optimization of the cylindrical parameters for the cone-pillar bi-structured SiC surfaces was conducted by Chen et al.<sup>24</sup> to guide subsequent experimental preparations, with the optimized parameters being a pitch of roughly 2  $\mu\text{m}$ , a diameter of 6  $\mu\text{m}$ , and a structural height of 8.3  $\mu\text{m}$ . Additionally, Genetic Algorithms and Topological Optimization are often used in the optimization process; however, these techniques are usually slow, inefficient, and can easily become stuck in a local optimum. In practical applications, to ensure a wide optimization parameter interval and improve the robustness of sample preparation, it is often necessary to design metamaterials inversely to achieve optimal microstructures according to desired spectral responses.<sup>25-30</sup> Nevertheless, this inverse problem is difficult to solve effectively as there is an implicit and sometimes non-unique relationship between

artificial structures and optical responses.

Machine Learning (ML) has recently become a powerful and innovative technique for complex computational problems and inverse design, i.e., to predict the complete optical response of photonic structures for given geometric parameters, as well as to retrieve the optimal design parameters for the desired optical response.<sup>31</sup> ML approach can be applied to strike the balance between excellent spectral characteristics and manufacture availability, which is beneficial to obtain easy-to-process artificial structures and hence to reduce the fabrication cost.<sup>32-34</sup> Additionally, ML is accurate and efficient in establishing correlations and sensitivities between numerous design variables, determining the optimal parameter interval and thus enhancing the robustness of the material preparation.<sup>35-37</sup> Therefore, by utilizing ML, we can incorporate it into the construction of biomimetic photonic structures to enhance spectral performance, clarify parametric mechanisms of action, and reduce the cost of preparation.

In this work, we introduce ML into the design and fabrication of a biomimetic photonic structure inspired by *Batocera Lineolata* Hope. Specifically, we construct three SiO<sub>2</sub> biomimetic metasurfaces (cylindrical array, truncated cone array, and cone array). ML was then used to intelligently learn the relation between the spectral properties and design parameters of different models. ML Results show that the truncated cone array is more sensitive to the height-to-diameter ratio (H/D) compared with other models, and thus exhibits better emissivity performance and more robust processability for the same aspect ratio. Additionally, the emissivity of SiO<sub>2</sub>

biomimetic metasurfaces constructed using reactive ion etching is comparable to that of the ML-prediction samples and exhibits impressive radiative cooling properties. Our model can provide possibilities for the inverse design of biomimetic photonic materials, opening up a new paradigm for the discovery of complex photonic structures. Moreover, the preparation of such robust radiative cooling metamaterials is an important contribution to the standardization of outdoor testing of passive radiative cooling.

## **2. Results and Discussions**

Spectral tests revealed that *Batocera Lineolata* Hope (BLH) forewings possess an impressive average emissivity of 0.93 in the 8-13  $\mu\text{m}$  band (Figure S1). Figure 1a illustrates that the forewings of BLH in the Chinese mountains have a golden sheen and are capable of regulating body temperature through thermal radiation. Scanning electron microscope (SEM) images show that the forewings of the BLH are covered by tiny villi (Figure 1b). The small villi show a cone-like shape with many prismatic ridges appearing on the surface of the cones, and this structure plays a key role in the mid-infrared wavelengths for anti-reflection, which is similar to the structure of the previously studied long-horned beetle (Figure 1c). As revealed by previous studies <sup>[19]</sup>, the special structure of the biological BLH model generates a gradual refractive index change, which allows it to exhibit high emissivity in the mid-infrared range. Following the appearance of biological prototypes, we split the biomimetic structures into three microarray models as in Figure 1d. Previous studies have largely focused on the thermal radiation mechanism, yet have neglected to investigate the correlation

between the sensitivity parameters and the spectral characteristics. Moreover, there is a lack of a well-balanced strategy between spectral performance optimization and practical processing robustness. To further explore this, machine learning methods could be employed.

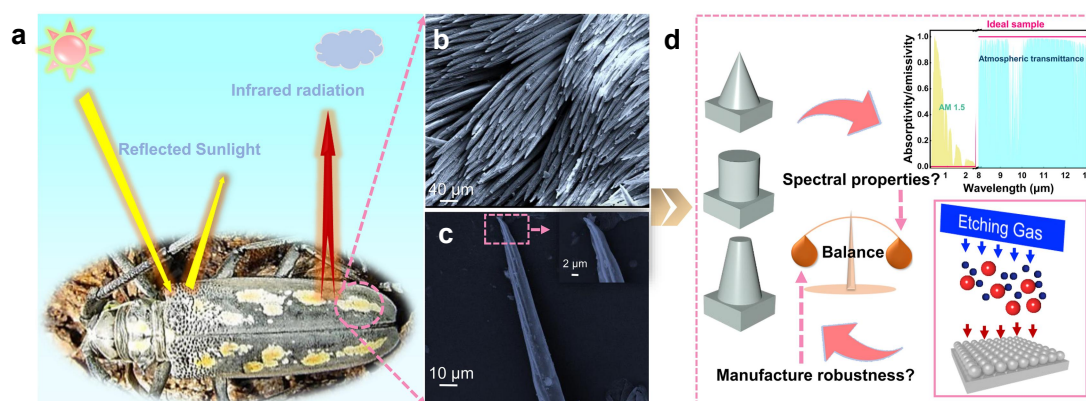


**Figure 1.** (a) Photograph and schematic diagram of temperature thermal regulation of a Batocera Lineolata Hope (BLH). (b) and (c) SEM images of the forewing of the BLH. (d) Microstructure array models derived from biological microscopic models.

Silicon dioxide ( $\text{SiO}_2$ ) was chosen as the optimal substrate material because of its convenience in micro/nanofabrication, its resistance to multiple environments, and the Si-O stretching vibrations that result in excellent infrared emission.<sup>38-40</sup> Inspired by the biological model, metasurfaces were designed with bulk  $\text{SiO}_2$  material used as the substrate and matrix material. Three typical structure models with metasurface cross-sections (i.e., cylindrical, truncated cone, and cone) are constructed and are shown in Figures 2a, 2d, and 2g. To obtain the emissivity corresponding to the three derived models, we apply finite-difference time-domain (FDTD) simulations for each periodic array model, with the specific boundary conditions shown in Figure S2. Through the parameter sweep results in Figure S3 and Figure 2b-c, it can be

determined that the highest emissivity is achieved when the cylindrical array has a diameter of 1.4  $\mu\text{m}$  and a height of 1.6  $\mu\text{m}$  (with a structured period of 2  $\mu\text{m}$ ), yielding an average emissivity of 0.96. For the truncated cone array, the highest average emissivity (0.985) is obtained from the parameter sweep results in Figure S4 and Figures 2e-f when the structure height is about 2.8  $\mu\text{m}$ , the diameter at the top is 1  $\mu\text{m}$  and the diameter at the bottom is 2  $\mu\text{m}$ . Further sweeps for the two structural elements of the cone array revealed that the best emissivity was achieved with a structure diameter of 2  $\mu\text{m}$  and a structure height of 5  $\mu\text{m}$ , with an average emissivity of approximately 0.99 (Figure S5 and Figure 2h-i). The parameter sweeping data indicates that truncated cone arrays and cone arrays demonstrate superior emissivity, thus we will focus on analyzing the structural parameters of the biomimetic metasurface based on these two structures.

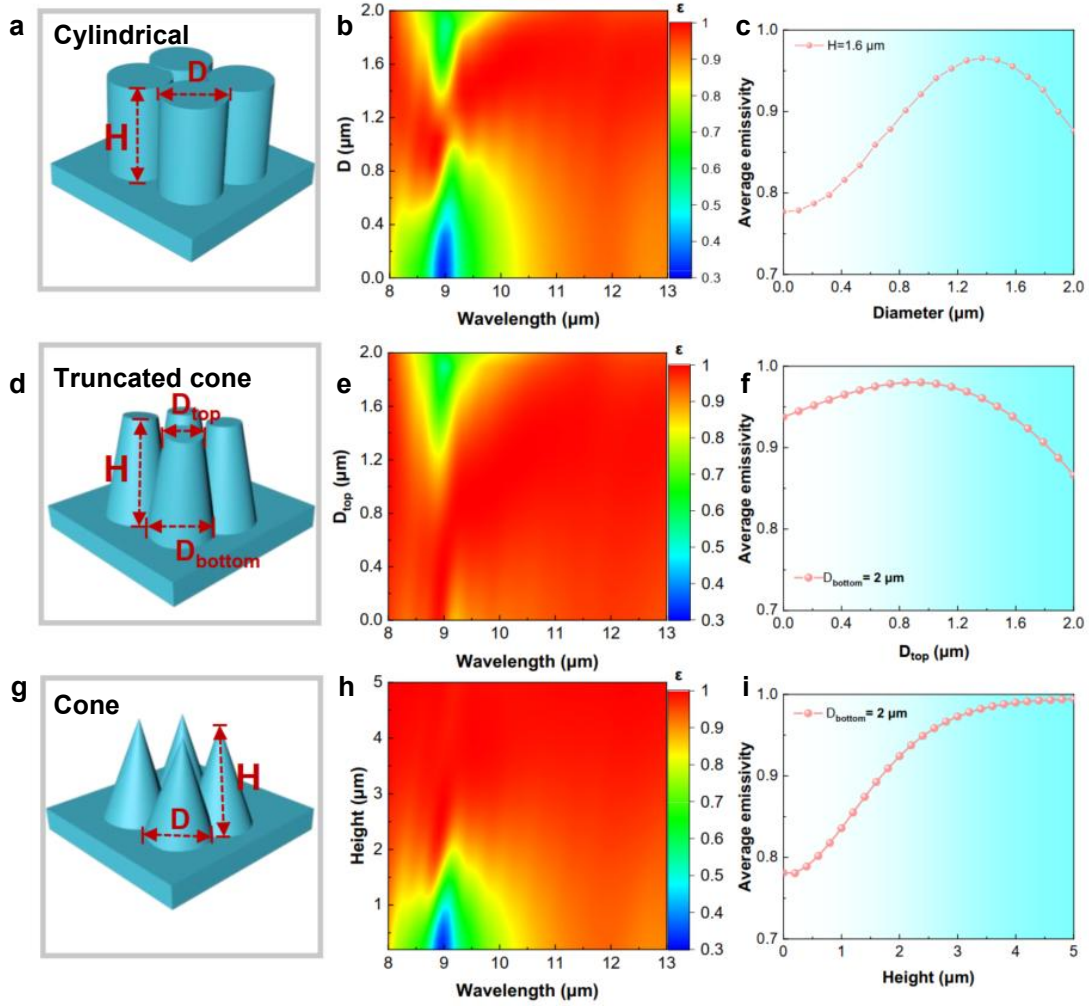


**Figure 2.** (a) Cylindrical model, (b) Emissivity map vs. cylindrical diameter, and (c) shows the corresponding average emissivity (8-13  $\mu\text{m}$  wavelength range) plots. (d) Truncated cone model, and (e) Emissivity map vs. truncated cone top diameter. (f) show the corresponding average emissivity (8-13  $\mu\text{m}$  wavelength range) plots. (g) Cone model, (h) Emissivity map vs. cone structure height, and (i) show the corresponding average emissivity (8-13  $\mu\text{m}$  wavelength range) plots.

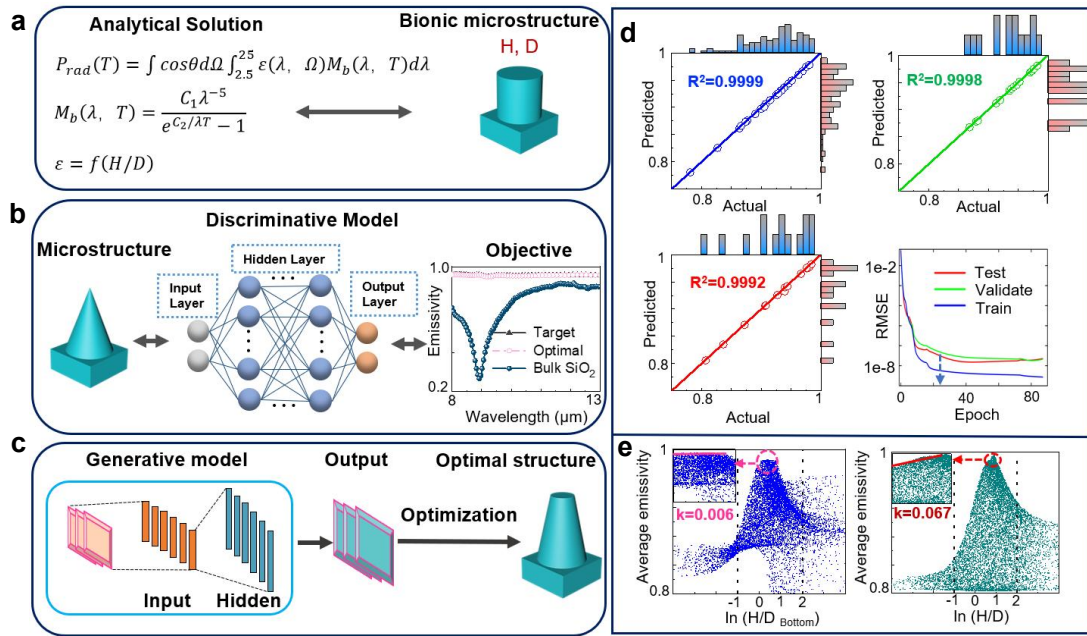
We demonstrate the general implementation of machine learning into the optimal design of biomimetic metamaterials in Figure 3. In principle, the optimal task can be fulfilled by analytical calculation combined with parametric sweeping, as shown in

Figure 3a. However, such traditional methods may yield a local optimal solution instead of the global one, and they are usually time-consuming for large optimization spaces. To accelerate the optimization process and explore optimal biomimetic microstructures, machine learning methodology is incorporated into the inverse design process. Herein we use a deep learning model to predict the spectral emissivity and inversely obtain optimal geometrical parameters for the target spectral response. The deep learning model is selected due to the non-uniqueness phenomenon of the spectral response: one identical spectral emissivity may be realized by multiple distinct geometrical parameters (also referred to as the degeneracy problem), which will result in convergence difficulties in neural networks that are fed with the spectral response and output the designed geometrical parameters. Figure 3b illustrates the deep learning model proposed for the generation and optimization of the SiO<sub>2</sub> metasurface. The proposed network is capable of both improving the accuracy of prediction and extending the model's functionality through its master network, which facilitates the flow of data in the forward path. Such a model provides a promising platform to intelligently learn the intrinsic and non-intuitive relation between biomimetic structures and their optical response from only a few training samples, thereby circumventing the laborious and step-by-step numerical simulations in traditional metamaterial design. We establish an initial training dataset, composed of 200 samples obtained from FDTD simulations, to train the deep learning model. The dataset is split into three groups: for training (80%), for validation (10%), and for final testing (10%), respectively. Levenberg-Marquardt algorithm is used as the training

algorithm. ML prediction results agree very well with the actual values, demonstrating the accuracy of the trained deep learning model (Figure 3d). Mean square errors (MSE) are chosen as the loss functions between the predicted and desired output, which is displayed with the variation of iterations. The loss functions show rapid convergence after around 24 epochs, implying the completion of the training phase. In addition, the three loss functions match well with each other, indicating that no overfitting problem is encountered.

Due to the degeneracy problem, the backward mapping from spectral responses to the design geometrical parameters is intractable and requires additional processing. To tackle this challenge, we encode the biomimetic microstructures into a compact representation using the well-trained generative model and produce many more biomimetic microstructures (here 10,000 samples) that are highly “similar” to the structures in the initial training dataset. Optimal microstructures are exhaustively searched and obtained from the compact representation. Optimal structural parameters are obtained for cylinders ( $H = 1.71 \mu\text{m}$ ,  $D = 0.28 \mu\text{m}$ ), truncated cones ( $H = 2.87 \mu\text{m}$ ,  $D_{\text{bottom}} = 1.96 \mu\text{m}$ ,  $D_{\text{top}} = 0.91 \mu\text{m}$ ), and cones ( $H = 4.97 \mu\text{m}$ ,  $D = 1.99 \mu\text{m}$ ), corresponding to average emissivities of 0.96, 0.985, and 0.99, respectively, as shown in Figure S6. We further identify the relationship between design parameters and emission properties for truncated cone arrays, revealing the structural effects on design principles. Figure 3e reveals a flatter optimization interval ( $H/D_{\text{bottom}}$  between 0.8 and 2.4) for truncated cones, compared to the cone arrays, with the slope estimated to be around 0.006 in the top optimal interval, as opposed to 0.067. This

wider space of optimal parameters will boost the preparation material's robustness. In addition, the slopes of the truncated cone array and the cone array on the left sides of the fitting curves are 0.15 and 0.12 (Figure S7), respectively, indicating that the truncated cones are more sensitive to variations of H/D and will display superior average emissivity performance when the same aspect ratio is considered. Therefore, we can primarily conclude that the truncated conical array design is a better candidate to achieve optimal emission properties.



**Figure 3.** Photonic design methodologies with machine learning incorporated. (a) Optimal design through analytical calculation or simple parametric sweeping. Such a strategy may not yield satisfactory results, especially for large solution spaces. (b) A discriminative model that learns the bidirectional mapping of the biomimetic metamaterials and corresponding spectral responses. Note that backward mapping from spectral responses to structural parameters can be challenging due to degeneracy problems. (c) A trained generative model produces far more biomimetic structures that

are similar to the initial training samples. Global optimal solutions are searched and located from this newly generated extended space, thus avoiding the backward mapping and degeneracy problem. (d) The accuracy of the trained deep learning model. (e) Machine learning prediction intensive parameter point: the average emissivity corresponding to the height-to-diameter ratio ( $\ln(H/D_{\text{bottom}})$ ) of the truncated cone array (left), and the average emissivity corresponding to the height-to-diameter ratio ( $\ln(H/D)$ ) of cone array (right).

To gain a better understanding of the results, Figures 4a and 4b illustrate the relevant distribution of the electric field at the resonance wavelength of 9.3  $\mu\text{m}$ . The four optimized truncated cone structures are the fundamental structural units, as demonstrated in the figures. The electric field enhancement is localized around the truncated cones, thus resulting in an increase in the emissivity of the  $\text{SiO}_2$  sample with a metasurface due to the more efficient activation of phonon polarization excitons. Moreover, at a resonance wavelength of 9.3  $\mu\text{m}$ , the real part of the dielectric constant ( $\text{Re}(\epsilon)$ ) is less than -1 (Figure S8), resulting in the near-complete absorption of the incident electromagnetic wave due to the excitation of surface plasmon polaritons (SPPs) between the cones. This is evidenced by the electric field distributions in Figures 4c and 4d, which are strongly confined to the gaps between the cones. Figure S9 indicates that for microstructured arrays with tilted surfaces, a gradual refractive index change is usually present, which boosts the emission from the sample surface. This finding is further supported by the resistive loss ( $Q$ ) distribution plot at 9.3  $\mu\text{m}$  wavelength (Figure S10).

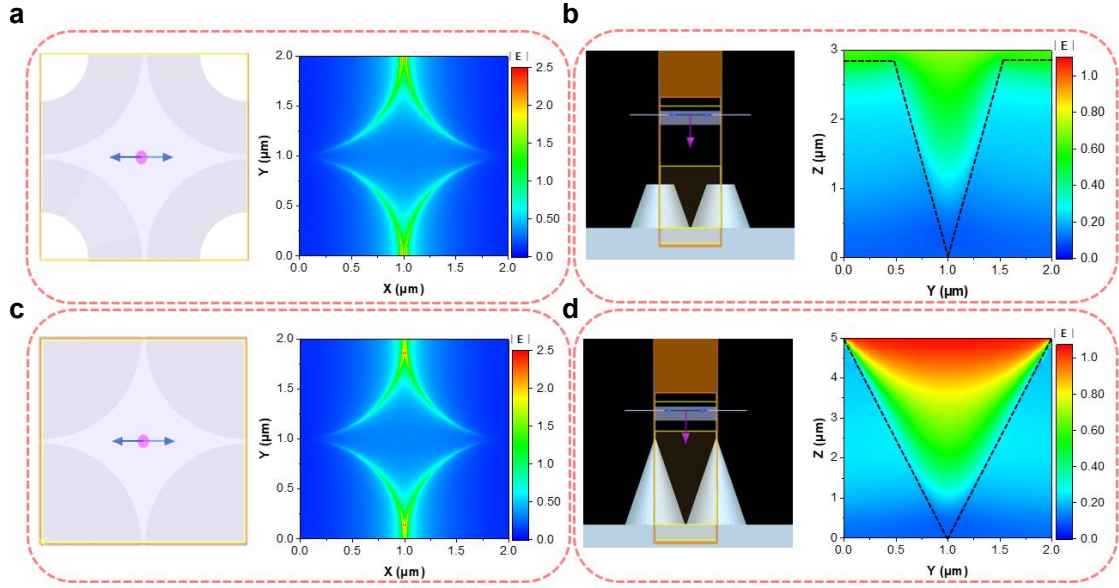


**Figure 4.** Electric field distribution of SiO<sub>2</sub> with truncated cone array at a resonant single wavelength (9.3 μm): (a) X-Y plane, (b) X-Z plane. Electric field distribution of SiO<sub>2</sub> with cone array at a resonant single wavelength (9.3 μm): (c) X-Y plane, (d) X-Z plane.

We conducted meticulous preparations of varied models to ensure their practical applicability. Figure 5 presents SEM images of the samples under different preparation conditions, both in-plane and cross-section, with the Height (H), Diameter (D), Aspect ratio (H/D), and the corresponding average emissivity of each sample displayed in the inset. Results from Figures 5(a)-(e) indicate that cylindrical arrays with higher aspect ratios have an average emissivity of more than 0.9, while truncated cone arrays, which are easier to manufacture, exhibit an average emissivity of more than 0.93 for varied aspect ratios and are highly robustness in their production (Figures 5(f)-(j)). It has been established in previous studies that the effect of disorder on the emissivity of the constructed truncated cone structure is relatively weak. [23]

However, the microstructured samples of cone arrays have exhibited poor emissivity performance due to the height restrictions of the fabrication, as demonstrated in Figures 5(k)-(o). The above results indicate that the difficulty of fabricating cylindrical and conical arrays with sizes close to the ML-optimized size due to the limitations of existing preparation techniques and fabrication precisions leads to lower-than-expected emissivity. It also demonstrates that the truncated cone model has a higher emissivity and a more robust processability, which is consistent with the results of the ML sensitivity analyses. Additionally, the study also demonstrated that different batches of truncated cone samples had a high IR emissivity, which is a beneficial characteristic for standardizing radiative cooling devices.

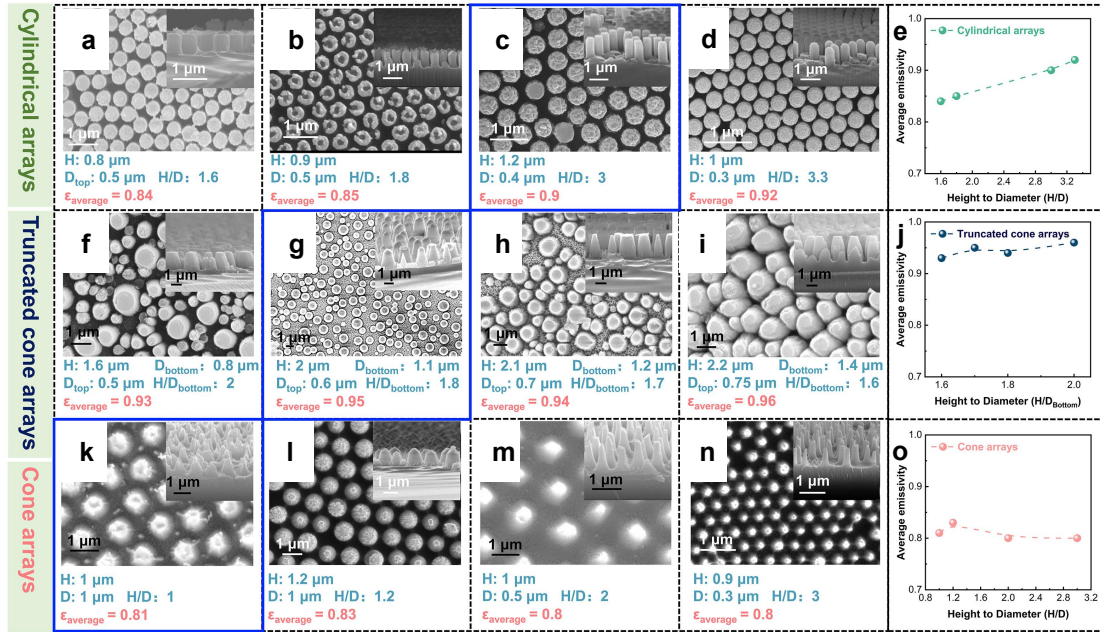


**Figure 5.** Samples prepared under different conditions: Constructions of cylindrical arrays are counted in Figures 5(a)-(d), (e) the corresponding average emissivity; constructions of truncated cone arrays are counted in Figures 5(f)-(i), (j) the corresponding average emissivity; and constructions of cone arrays are counted in

Figures 5(k)-(n), (o) the corresponding average emissivity.

To verify the accuracy of the learning results, three different SiO<sub>2</sub> metasurface samples from Figure 5 (blue wireframes were marked) were tested, and the spectra were compared to the results of ML. The emissivity spectra of the prepared samples, as shown in Figures 6a-c, generally demonstrate a marked increase in emissivity compared to bulk SiO<sub>2</sub> (0.79), with an average emissivity of 0.9 for the cylindrical array samples, 0.95 for the truncated cone array samples, and 0.81 for the cone array samples, which are almost identical to the results of ML. Therefore, the truncated cone sample is selected as the typical example to validate the radiative cooling effects. IR thermography measurements were applied to the monitoring of surface temperature samples with the metasurface. The test setup is depicted in Figure 6d, wherein each small test chamber is made of a transparent polyethylene sheet, with a vent on the front side and the other three sides wrapped with aluminum foil. The test chambers, which are small in size, are situated atop the insulating foam, and various samples are consecutively placed on the top of the chambers. To complete the experimental verification process, miniature figurines made of polystyrene are inserted into the test chamber. At the start (0 min), the surface temperature of all miniature figurines remained almost the same. Upon attaining thermal equilibrium (30 min), the miniature figurine situated on the metasurface was 8.3 °C cooler than the one placed in bulk SiO<sub>2</sub> and 2.2 °C cooler than the one placed in silver-plated SiO<sub>2</sub> (Figure 6e). The reflectance of the SiO<sub>2</sub> samples with the metasurface in the solar band (0.25-2.5 μm) and the theoretical radiative cooling capacity were examined and

calculated (Figure S11). It was observed that the SiO<sub>2</sub> samples with the metasurface showed more than 95% reflectance and a cooling capacity of 8.5 °C (non-radiative cooling coefficient  $h = 12 \text{ W m}^{-1}$ ), which is close to the experimentally verified results (8.3 °C). Results demonstrate that the SiO<sub>2</sub> samples with the metasurface are highly effective in achieving radiative cooling. Furthermore, the truncated cone samples were remarkably hydrophobic in comparison to the bulk SiO<sub>2</sub> samples, which is an advantageous characteristic for outdoor utilization (Figure S12).

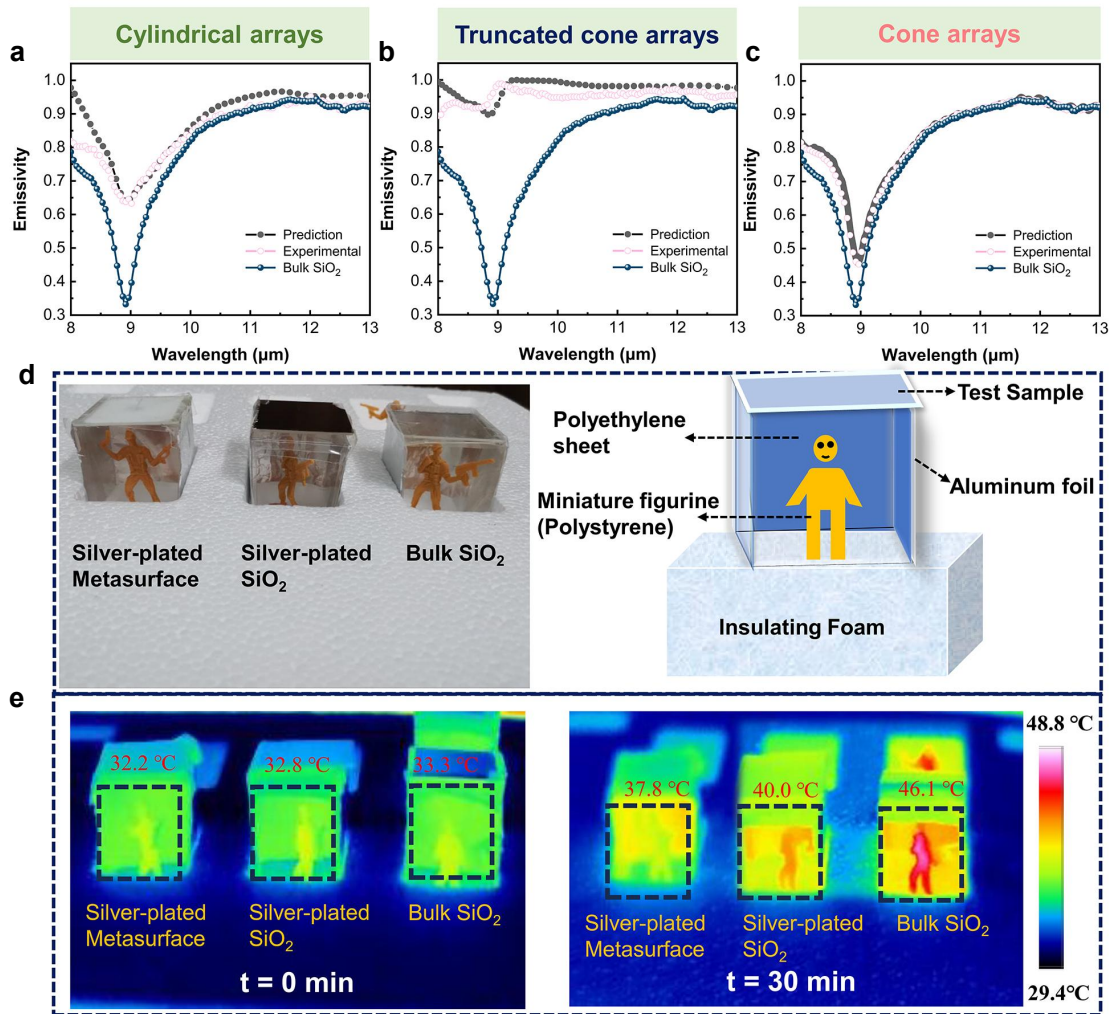


**Figure 6.** The simulated and experimental IR emissivity spectra (8-13 μm) of SiO<sub>2</sub> samples (From the blue wireframe marker samples in Figure 5) with (a) cylindrical arrays, (b) truncated cone arrays, and (c) cone arrays. (d) Optical photographs of

samples tested for infrared thermography (from left to right, silver-plated metasurface (truncated microcone array samples), silver-plated SiO<sub>2</sub> sample, and Bulk SiO<sub>2</sub> sample) and schematic diagram of the outdoor test setup. (e) Infrared thermography of different samples exposed to direct sunlight for a period of 0 min and 30 min.

### **3. Conclusion**

In this paper, we present a deep generative model that is capable of addressing the biomimetic metamaterial design problem. A discriminative model is developed to learn the bidirectional mapping between biomimetic metamaterials and their corresponding spectral responses. To avoid degeneracy issues, we encode the metamaterial design into a large latent space, which leads to a probabilistic representation of the metamaterial. This allows us to search for and locate optimal structures in the latent space, thus solving the one-to-many mapping problem in the inverse direction. Our proposed method yielded optimal structural parameters for cylinders, truncated cones, and cones, resulting in an average emissivity of 0.96, 0.985, and 0.99, respectively. This is a significant improvement compared to pure SiO<sub>2</sub> materials and even compared to imitative creatures. The improved spectral emissivity was verified through simulations and experiments. We fabricated truncated microcone array samples and experimentally demonstrated their excellent radiative cooling performance. Experimental and ML studies have demonstrated that truncated cone arrays are highly robust for increasing the emissivity of SiO<sub>2</sub>. Our proposed fabrication method for biomimetic metamaterials can expedite the process of designing and optimizing robust radiative cooling metamaterials, making them

suitable for standardized passive radiation cooling applications. This data-driven approach is an efficient technique that can be used to expedite the design, optimization, and discovery of biomimetic metamaterials, photonic devices, and radiative manipulation capabilities.

#### **4. Experimental section**

*Materials:* This work employed a 40×40×1 mm<sup>3</sup> quartz (SiO<sub>2</sub>) block sourced from Aladdin Company. Silver ingot particles (Ag) were procured from Tim (Beijing) New Materials Technology Co. Ltd. whereas analytical grade chemicals such as ethanol (C<sub>2</sub>H<sub>5</sub>OH), polystyrene spheres (PS), sodium dodecylbenzene sulfate (SDS) and acetone (CH<sub>3</sub>COCH<sub>3</sub>) were obtained from Tianjin Tianli Chemical Reagent Co. The etching process was facilitated by argon (Ar, 99.99%), nitrogen (N<sub>2</sub>, 99.99%), and trifluoromethane (CHF<sub>3</sub>, 99.99%) provided by Harbin Liming Gas Co.

*Preparation of SiO<sub>2</sub> Metasurface (cylindrical arrays, truncated conical arrays, conical arrays):* For the fabrication of SiO<sub>2</sub> metasurfaces, such as cylindrical arrays, and truncated conical arrays, annealed silver micro-nanospheres are used as the etching mask. The size of the silver spheres can be adjusted by controlling the thickness of the silver, and the period of the silver spheres can be regulated by adjusting the annealing time and temperature (550 °C with a holding time of 2 hours). Additionally, for the construction of cylindrical arrays, and conical arrays, liquid surface self-assembled microspheres of 2 μm polystyrene (PS) are used to construct the mask. Further details of the experimental methodology can be found in prior studies.<sup>23, 41</sup>

*Characterization and Measurements:* A SIGMA 300 Scanning Electron Microscope (SEM) (Zeiss, Germany) was utilized to evaluate the micromorphology of the prepared samples. A Fourier Transform Infrared Spectrometer (FTIR) with an A562 Integrating Sphere was employed to measure the infrared spectral reflectance of the samples within the wavelength range of 2.5 to 25  $\mu\text{m}$ . Additionally, a Tix660 Infrared Thermal Imager (Fluke) was used to capture thermal images of the samples in the spectral range of 7.5-14  $\mu\text{m}$ .

*Simulation:* The spectral properties of the designed emitter were calculated using the Finite-Difference Time-Domain (FDTD) method for electromagnetic waves from the Lumerical software package. Parametric sweeping of all metasurface structures was conducted using the same method, with a plane-wave light source for illumination, whose propagation and polarization directions were along the negative Z and X axes, respectively. Periodic boundary conditions were set in the X- and Y-axes and Perfectly Matched Layer boundary conditions were set along the Z-axis. The mesh type was a uniform mesh, with the maximum mesh step set to 25 nm and the auto-off value set to  $1\text{e}^{-5}$ . The dielectric constants of Ag and  $\text{SiO}_2$  were taken from Palik (1991).

*Machine Learning:* Artificial neuron network (ANN) and Gaussian process regression (GPR) have both been employed in this study. ANN and GPR are well-established data-driven techniques for building ML models of biomimetic metamaterials. Artificial neural networks, inspired by neurons in biological brains, are built on collections of connected units called artificial neurons. GPR depends on the

assumption that the uncertain predictive function is modeled by sampling from a multivariate Gaussian distribution and maintaining the posterior distribution upon observation.<sup>42</sup> Other machine learning algorithms, such as random forest and support vector models are tested with the initial dataset for their performance. We use the coefficient of determination ( $R^2$ ) and root-mean-square errors ( $RMSE$ ) to evaluate the reliability of the established models, which are defined as

$$R^2 = 1 - \frac{\sum_{i=1}^m (y_i - y'_i)^2}{\sum_{i=1}^m (y_i - y''_i)^2}$$

and

$$RMSE = \sqrt{\frac{\sum_{i=1}^m (y_i - y'_i)^2}{m}}$$

where  $y_i$  and  $y'_i$  are respectively the actual value and predicted value over the same sample,  $y''_i$  is the mean value of objective functions and  $m$  is the total number of sampling points. Results show that the GPR model has the smallest value of root-mean-square deviation, i.e., the performance of the GPR model is optimal compared with other machine learning models.

### **Author Information**

Corresponding Author

Qingxiang Ji - *Center for Composite Materials and Structure, Harbin Institute of Technology, Harbin, 150001, China. E-mail: jiqingxiang@hit.edu.cn*

Hongbo Xu - *School of Chemistry and Chemical Engineering, Harbin Institute of Technology, Harbin, 150001, PR China. E-mail: iamxhb@hit.edu.cn*

Jiupeng Zhao - *School of Chemistry and Chemical Engineering, Harbin Institute of Technology, Harbin, 150001, PR China. E-mail: jpzhao@hit.edu.cn*

**Authors**

Zhenmin Ding - *School of Chemistry and Chemical Engineering, Harbin Institute of Technology, Harbin, 150001, PR China*

Xin Li - *School of Chemistry and Chemical Engineering, Harbin Institute of Technology, Harbin, 150001, PR China*

Yunce Zhang - *Center for Composite Materials and Structure, Harbin Institute of Technology, Harbin, 150001, China*

Honglin Li - *School of Chemistry and Chemical Engineering, Harbin Institute of Technology, Harbin, 150001, PR China*

Hulin Zhang - *Center for Composite Materials and Structure, Harbin Institute of Technology, Harbin, 150001, China*

Lorenzo Pattelli - *Istituto Nazionale di Ricerca Metrologica (INRiM), Turin, 10135, Italy; European Laboratory for Non-linear Spectroscopy (LENS), Sesto Fiorentino, 50019, Italy*

Yao Li- *Center for Composite Materials and Structure, Harbin Institute of Technology, Harbin, 150001, China; Suzhou Laboratory, Suzhou, 215123, PR China*

### **Author Contributions**

H. Xu presents a conceptualization. Y. Li provides the resources and funding acquisition. Z. Ding initiated this project and wrote the first draft. X. Li, H. Zhang, and H. Li provided the simulated data calculated by FDTD software. Y. Zhang and Q. Ji implemented the machine learning process. Q. Ji, J. Zhao, and L. Pattelli revised the manuscript. All authors discussed the results and contributed to the writing.

### **Supporting Information**

The Supporting Information is available free of charge on the ACS Publications website at DOI: xxxxx.

Basic optical characteristics of *Batocera Lineolata* forewings; design and numerical methods; Machine learning prediction results; Investigation of simulation

spectral performance of different experimental models; Simulation of electric field distribution; Theoretical cooling calculation; Hydrophobicity analysis of sample.

## Notes

The authors declare no competing financial interest.

## Acknowledgments

We thank the National Key R&D Program of China (2022YFB3902704), the National Natural Science Foundation of China (No.52072096, 12302169), the Natural Science Foundation of Heilongjiang Province Heilongjiang (LH2023E034), and the Fundamental Research Funds for the Central Universities (HIT OCEF. 2021004).

## References

- (1) Fan, S.; Li, W. Photonics and thermodynamics concepts in radiative cooling. *Nat. Photonics* **2022**, *16* (3), 182-190.
- (2) Lee, M.; Kim, G.; Jung, Y.; Pyun, K. R.; Lee, J.; Kim, B. W.; Ko, S. H. Photonic structures in radiative cooling. *Light Sci Appl.* **2023**, *12* (1), 134.
- (3) Zhang, Y.; Chen, X.; Cai, B.; Luan, H.; Zhang, Q.; Gu, M. Photonics Empowered Passive Radiative Cooling. *Adv. Photon. Res.* **2021**, *2* (4), 2000106.
- (4) Yu, K.; Fan, T.; Lou, S.; Zhang, D. Biomimetic optical materials: Integration of nature's design for manipulation of light. *Prog. Mater. Sci.* **2013**, *58* (6), 825-873.
- (5) Xiong, R.; Wu, W.; Lu, C.; Colfen, H. Bioinspired Chiral Template Guided Mineralization for Biophotonic Structural Materials. *Adv. Mater.* **2022**, *34* (51), e2206509.

- (6) Henrion, W.; Tributsch, H. Optical solar energy adaptations and radiative temperature control of green leaves and tree barks. *Sol. Energ. Mater. Sol. C.* **2009**, *93* (1), 98-107.
- (7) Krishna, A.; Nie, X.; Warren, A. D.; Llorente-Bousquets, J. E.; Briscoe, A. D.; Lee, J. Infrared optical and thermal properties of microstructures in butterfly wings. *Proc. Natl. Acad. Sci. USA* **2020**, *117* (3), 1566-1572.
- (8) Osotsi, M. I.; Zhang, W.; Zada, I.; Gu, J.; Liu, Q.; Zhang, D. Butterfly wing architectures inspire sensor and energy applications. *Natl. Sci. Rev.* **2021**, *8* (3), nwaa107.
- (9) Perez-de la Fuente, R.; Delclos, X.; Penalver, E.; Speranza, M.; Wierzechos, J.; Ascaso, C.; Engel, M. S. Early evolution and ecology of camouflage in insects. *Proc. Natl. Acad. Sci. USA* **2012**, *109* (52), 21414-21419.
- (10) Cheng, Z.; Han, H.; Wang, F.; Yan, Y.; Shi, X.; Liang, H.; Zhang, X.; Shuai, Y. Efficient radiative cooling coating with biomimetic human skin wrinkle structure. *Nano Energy* **2021**, *89*, 106377.
- (11) Zhou, H.; Xu, J.; Liu, X.; Zhang, H.; Wang, D.; Chen, Z.; Zhang, D.; Fan, T. Bio-Inspired Photonic Materials: Prototypes and Structural Effect Designs for Applications in Solar Energy Manipulation. *Adv. Funct. Mater.* **2017**, *28* (24), 1705309.
- (12) Zhao, D.; Aili, A.; Zhai, Y.; Xu, S.; Tan, G.; Yin, X.; Yang, R. Radiative sky cooling: Fundamental principles, materials, and applications. *Appl. Phys. Lett.* **2019**, *6* (2), 0213061.

- (13) Chen, M.; Pang, D.; Chen, X.; Yan, H.; Yang, Y. Passive daytime radiative cooling: Fundamentals, material designs, and applications. *EcoMat* **2021**, *4* (1), e12153.
- (14) Norman Nan Shi; Cheng-Chia Tsai; Fernando Camino; Gary D. Bernard; Nanfang Yu; Wehner, R. Keeping cool: Enhanced optical reflection and radiative heat dissipation in Saharan silver ants. *Science* **2015**, *349* (6245), 298-301.
- (15) Xie, D.; Yang, Z.; Liu, X.; Cui, S.; Zhou, H.; Fan, T. Broadband omnidirectional light reflection and radiative heat dissipation in white beetles *Goliathus goliatus*. *Soft Matter* **2019**, *15* (21), 4294-4300.
- (16) Didari, A.; Menguc, M. P. A biomimicry design for nanoscale radiative cooling applications inspired by *Morpho didius* butterfly. *Sci. Rep.* **2018**, *8* (1), 16891.
- (17) Tang, C. F.; Li, F. F.; Cao, Y.; Liao, H. J. Universal cooling patterns of the butterfly wing scales hierarchy deduced from the heterogeneous thermal and structural properties of *Tirumala limniace* (Lepidoptera: Nymphalidae, Danainae). *Insect. Sci.* **2022**, *29* (6), 1761-1772.
- (18) Liu, X.; Xiao, C.; Wang, P.; Yan, M.; Wang, H.; Xie, P.; Liu, G.; Zhou, H.; Zhang, D.; Fan, T. Biomimetic Photonic Multiform Composite for High-Performance Radiative Cooling. *Adv. Opt. Mater.* **2021**, *9* (22), 2101151.
- (19) Zhang, H.; Ly, K. C. S.; Liu, X.; Chen, Z.; Yan, M.; Wu, Z.; Wang, X.; Zheng, Y.; Zhou, H.; Fan, T. Biologically inspired flexible photonic films for efficient passive radiative cooling. *Proc. Natl. Acad. Sci. USA* **2020**, *117* (26), 14657-14666.
- (20) Deinega, A.; John, S. Effective optical response of silicon to sunlight in the

finite-difference time-domain method. *Opt. Lett.* **2012**, *37* (1 ), 112-114.

(21) Amirjani, A.; Sadrnezhad, S. K. Computational electromagnetics in plasmonic nanostructures. *J. Mater. Chem. C* **2021**, *9* (31), 9791-9819.

(22) Wu, K.; Coquet, P.; Wang, Q. J.; Genevet, P. Modelling of free-form conformal metasurfaces. *Nat. Commun.* **2018**, *9* (1), 3494.

(23) Ding, Z.; Pattelli, L.; Xu, H.; Sun, W.; Li, X.; Pan, L.; Zhao, J.; Wang, C.; Zhang, X.; Song, Y.; et al. Iridescent Daytime Radiative Cooling with No Absorption Peaks in the Visible Range. *Small* **2022**, e2202400.

(24) Chen, D.; Dong, J.; Yang, J.; Hua, Y.; Li, G.; Guo, C.; Xie, C.; Liu, M.; Liu, Q. Realization of near-perfect absorption in the whole reststrahlen band of SiC. *Nanoscale* **2018**, *10* (20), 9450-9454.

(25) Zhang, Y.; Ma, Z.; Zhang, X.; Wang, T.; Choi, H. W. Optically pumped whispering-gallery mode lasing from 2- $\mu$ m GaN micro-disks pivoted on Si. *Appl. Phys. Lett.* **2014**, *104* (22), 221106.

(26) Ma, W.; Cheng, F.; Xu, Y.; Wen, Q.; Liu, Y. Probabilistic Representation and Inverse Design of Metamaterials Based on a Deep Generative Model with Semi-Supervised Learning Strategy. *Adv. Mater.* **2019**, *31* (35), e1901111.

(27) Zhang, M.; Poumirol, J.-M.; Chery, N.; Majorel, C.; Demoulin, R.; Talbot, E.; Rinnert, H.; Girard, C.; Cristiano, F.; Wiecha, P. R.; et al. Infrared nanoplasmonic properties of hyperdoped embedded Si nanocrystals in the few electrons regime. *Nanophotonics* **2022**, *11* (15), 3485-3493.

(28) Weifeng Jiang , Y. Z., Guofu Yin, Houhong Lu, Luofeng Xie, Ming Yin.

Dispersion relation prediction and structure inverse design of elastic metamaterials via deep learning. *Mater. Today Phys.* **2022**, 22, 2542-5293.

(29) Chen, Y.; Zhu, J.; Xie, Y.; Feng, N.; Liu, Q. H. Smart inverse design of graphene-based photonic metamaterials by an adaptive artificial neural network. *Nanoscale* **2019**, 11 (19), 9749-9755.

(30) Liu, Z.; Zhu, D.; Raju, L.; Cai, W. Tackling Photonic Inverse Design with Machine Learning. *Adv. Sci. (Weinh)* **2021**, 8 (5), 2002923.

(31) Wang, Z.; Sobey, A. A comparative review between Genetic Algorithm use in composite optimisation and the state-of-the-art in evolutionary computation. *Compos. Struct.* **2020**, 233, 111739.

(32) Gok, E. C.; Yildirim, M. O.; Haris, M. P. U.; Eren, E.; Pegu, M.; Hemasiri, N. H.; Huang, P.; Kazim, S.; Uygun Oksuz, A.; Ahmad, S. Predicting Perovskite Bandgap and Solar Cell Performance with Machine Learning. *Sol. RRL* **2021**, 6 (2), 2100927.

(33) Purnawati, D.; Regonia, P. R.; Bermundo, J. P.; Ikeda, K.; Uraoka, Y. Machine-Learned Fermi Level Prediction of Solution-Processed Ultrawide-Bandgap Amorphous Gallium Oxide (a-Ga<sub>2</sub>O<sub>x</sub>). *ACS Appl. Electron. Mater.* **2022**, 4 (12), 5838-5846.

(34) Queralto, A.; Pacheco, A.; Jimenez, N.; Ricart, S.; Obradors, X.; Puig, T. Defining inkjet printing conditions of superconducting cuprate films through machine learning. *J. Mater. Chem. C* **2022**, 10 (17), 6885-6895.

(35) Liu, X.; Wang, P.; Xiao, C.; Fu, L.; Xu, J.; Zhang, D.; Zhou, H.; Fan, T. Compatible Stealth Metasurface for Laser and Infrared with Radiative Thermal

Engineering Enabled by Machine Learning. *Adv. Funct. Mater.* **2023**, *33* (11), 2212068.

(36) Ma, W.; Xu, Y.; Xiong, B.; Deng, L.; Peng, R. W.; Wang, M.; Liu, Y. Pushing the Limits of Functionality-Multiplexing Capability in Metasurface Design Based on Statistical Machine Learning. *Adv. Mater.* **2022**, *34* (16), e2110022.

(37) Zhou, T.; Jiang, S.; Han, T.; Zhu, S.-P.; Cai, Y. A physically consistent framework for fatigue life prediction using probabilistic physics-informed neural network. *Int. J. Fatigue* **2023**, *166*, 107234.

(38) Zhu L.; Raman A.; Wang, K. X.; Anoma, M. A.; Fan, S. Radiative cooling of solar cells. *Optica* **2014**, *1* (1), 32-38.

(39) Jaramillo-Fernandez, J.; Whitworth, G. L.; Pariente, J. A.; Blanco, A.; Garcia, P. D.; Lopez, C.; Sotomayor-Torres, C. M. A Self-Assembled 2D Thermofunctional Material for Radiative Cooling. *Small* **2019**, *15* (52), e1905290.

(40) Sun, Y.; He, H.; Huang, X.; Guo, Z. Superhydrophobic SiO<sub>2</sub>-Glass Bubbles Composite Coating for Stable and Highly Efficient Daytime Radiative Cooling. *ACS Appl. Mater. Inter.* **2023**, *15* (3), 4799-4813.

(41) Xu, H.; Liu, L.; Teng, F.; Lu, N. Emission Enhancement of Fluorescent Molecules by Antireflective Arrays. *Research (Wash D C)* **2019**, *2019*, 3495841.

(42) Schmidt, J.; Marques, M. R. G.; Botti, S.; Marques, M. A. L. Recent advances and applications of machine learning in solid-state materials science. *Npj Comput. Mater.* **2019**, *5* (1), 83.